AGU PUBLICATIONS

JGR

Journal of Geophysical Research: Space Physics

RESEARCH ARTICLE
10.1002/2015JA022291

Special Section:
Energetic Electron Loss and its Impacts on the Atmosphere

Model studies of short-term variations induced in trace gases by particle precipitation in the mesosphere and lower thermosphere

T. Fytterer[1], S. Bender[1], U. Berger[2], H. Nieder[1], M. Sinnhuber[1], and J. M. Wissing[3]

[1]Institute for Meteorology and Climate Research, Karlsruhe Institute of Technology, Eggenstein-Leopoldshafen, Germany, [2]Leibnitz-Institute of Atmospheric Physics, Kühlungsborn, Germany, [3]Institut für Umweltfoschung, Universität Osnabrück, Osnabrück, Germany

Key Points:
- The 27 day solar rotational signal in atmospheric trace gas simulations induced by particle precipitation
- Strong impact on trace gas response due to dynamical variability
- Overestimation of particle impact but qualitatively captured chemistry involved in the model

Correspondence to:
T. Fytterer,
tilo.fytterer@kit.edu

Citation:
Fytterer, T., S. Bender, U. Berger, H. Nieder, M. Sinnhuber, and J. M. Wissing (2016), Model studies of short-term variations induced in trace gases by particle precipitation in the mesosphere and lower thermosphere, *J. Geophys. Res. Space Physics*, *121*, 10,431–10,447, doi:10.1002/2015JA022291.

Received 21 DEC 2015
Accepted 30 SEP 2016
Accepted article online 6 OCT 2016
Published online 25 OCT 2016

Abstract The 3-D global chemistry and transport model (3dCTM) was used to investigate NO, OH, and O_3 from January 2002 to May 2010 between 60 km and 133 km. Their daytime and nighttime mean zonal means (55°–75° geomagnetic latitude) were analyzed with respect to short-term variations associated with particle precipitation. The corresponding ionization rates were derived from the 3-D atmospheric ionization module Osnabrück (AIMOS), which is based on particle flux measurements. The trace gas variations with respect to their background were investigated by using a superposed epoch analysis. The 27 day signature associated with particle precipitation is found in NO, while it is only indicated in OH and O_3 during winter. A varying solar spectrum associated with the 11 year solar cycle causes modifications of this signal up to 10%, while the main patterns are conserved. Published observations show a clear 27 day signal, qualitatively agreeing with the model results at altitudes >70 km except for O_3 in Northern Hemisphere winter. Further differences occur with respect to the magnitude of the trace gas variations, primarily attributed to the different trace gas background and dynamical variations of the background atmosphere. Absolute OH variations are overestimated by the 3dCTM during winter, while the opposite is true for O_3. These differences might originate from an unknown offset in AIMOS, incorrect chemical reaction rates, a different background of H_2O and O_3, and the model dynamics. However, their nonlinear relationship and their altitude of largest response are qualitatively captured in Southern Hemisphere winter.

1. Introduction

Precipitating particles (protons, electrons, and rarely heavier ions) that influence the chemistry of the mesosphere and lower thermosphere (MLT) region primarily originate from the Sun and the Earth's radiation belts. Therefore, they are related to solar activity and solar wind variability, including corotating interactive regions (CIRs). The CIRs are generally caused by long-lived coronal holes which are dark regions in the Sun's corona with open magnetic field lines, releasing fast particle beams. Coronal holes are locked to the Sun's rotational period of about 27 days and are stable over several successive solar rotations. Consequently, the CIR impact on the MLT region is considered as a quasi-persistent feature. The CIRs occur more frequently outside solar maximum conditions [*Richardson et al.*, 2000] because their formation tends to be disrupted by coronal mass ejections during solar maximum. They further modulate the solar wind properties, leading to geomagnetic disturbances in the magnetosphere and in turn result in particle precipitation from the radiation belts. The high-energy particles that travel with the solar wind are actually deflected by the Earth's magnetic field, but they can enter the atmosphere at high geomagnetic latitudes and directly precipitate down to the MLT region.

Particle precipitation is mostly limited to the area inside the auroral oval at ~55°–75° geomagnetic latitudes and primarily causes ionization and excitation of the main atmospheric compounds N_2 and O_2. This eventually leads to the production of odd hydrogen ($HO_x = H + OH + HO_2$) [*Solomon et al.*, 1981] and odd nitrogen ($NO_x = N + NO + NO_2$) [*Nicolet*, 1965] via a cascade of complex chemical reactions. In principle both HO_x and NO_x production contributes to the catalytic O_3 depletion [*Sinnhuber et al.*, 2012]. In the mesosphere HO_x is assumed to play the dominant role on short time scales, while NO_x is more important for long-term O_3 variations in the stratosphere due to the relatively short (long) lifetime of HO_x (NO_x) [*Jackman et al.*, 2014]. Since O_3 is a major radiative heating and cooling source in the stratosphere and mesosphere, perturbations in O_3 can cause temperature variations and influences the thermally balanced wind field. Thus, a more accurate

knowledge about the particle precipitation impact on MLT chemistry and O_3 in particular is necessary to improve our understanding of the entire middle atmosphere.

While the 27 day response of atmospheric air compounds due to solar UV radiation had received a lot of attention during recent years [e.g., *Ruzmaikin et al*., 2007; *Shapiro et al*., 2012], observations of the 27 day solar rotational impact related to particle precipitation are relatively rare to our knowledge. *Friederich et al.* [2014] reported a clear 27 day signature in NO_2 nighttime measurements around the stratopause region during summer associated with geomagnetic activity. Further observations of daily NO at polar latitudes revealed a significant 27 day response to electron precipitation in the lower thermosphere in each hemisphere and season [*Hendrickx et al*., 2015]. A 27 day signal in mesospheric NO related to geomagnetic activity was also reported by *Sinnhuber et al.* [2016]. Recent analysis presented by *Fytterer et al.* [2015] showed a distinct particle induced 27 day solar rotational signal in mesospheric nighttime OH and O_3 satellite measurements during winter. These results have encouraged us to repeat their analysis with model simulations.

In this paper we analyze 3-D chemistry transport model simulations of the volume mixing ratios (vmrs) of several trace gases (NO, OH, and O_3), while using NO and OH as a proxy for NO_x and HO_x, respectively. Particle ionization rates used to drive the model are derived from the 3-D atmospheric ionization module Osnabrück which is based on observed proton, electron, and alpha-particle fluxes. We investigated trace gas variations with respect to the 27 day solar rotational signal associated with geomagnetic activity. We focus on auroral latitudes (55° to 75° geomagnetic latitudes), while considering the altitudes between 60 km and 133 km from January 2002 to May 2010. The analysis is individually carried out during both summer and winter conditions in each hemisphere. The results are compared with observations from literature [*Hendrickx et al*., 2015; *Fytterer et al*., 2015; *Sinnhuber et al*., 2016]. The aim of this study is to test whether the observed 27 day signal associated with particle precipitation and the O_3 response to single particle events can be reproduced by a model which is driven by measured particle fluxes. We further investigated a possible impact of the 11 year solar cycle, photoionization, and dynamical variations of the atmospheric background on the 27 day signal.

2. Numerical Modeling and Analysis

2.1. The 3-D Chemistry Transport Model Simulations

The global 3-D chemistry transport model (3dCTM) [*Sinnhuber et al*., 2012, Appendix 1] is based on the Bremen 3dCTM [e.g., *Wissing et al*., 2010]. The 3dCTM extends from the tropopause up to the lower thermosphere (~10–133 km) on 47 pressure levels with a vertical distance of about 3 km in the stratosphere and mesosphere, 2 km around the mesopause, and up to 7 km in the lower thermosphere. The horizontal spacing is given on a latitude × longitude grid of approximately 2.5° × 3.75°. Recent model updates provide variable H_2 and O_2 distributions, resulting in improved HO_x values and eventually leading to more accurate nighttime O_3 patterns at altitudes >60 km. The advection terms in the 3dCTM are calculated by applying the so-called second-order moments scheme [*Prather*, 1986]. A family approach for the chemical families O_x (= O + O^1D + O_3), NO_x (= N + NO + NO_2), HO_x (= H + OH + HO_2), BrO_x (= Br + BrO), ClO_x (= Cl + ClO + $2Cl_2O_2$), and CHO_x (= CH_3 + CH_3O_2 + CH_3OOH + CH_3O + HCO) is used in the stratosphere. In the MLT region, O_x, HO_x, and NO_x are not in photochemical equilibrium and the family approach was not applied.

The 3dCTM is driven by meteorological data provided by simulations of the 3-D dynamical Leibniz-Institute middle atmosphere (LIMA) model [*Berger*, 2008; *Lübken et al*., 2013]. The LIMA model is nudged to the European Center for Medium-Range Weather Forecasts reanalysis data set (ERA-40) until ~40 km and is completely free-running at altitudes above the stratopause. The LIMA model is especially designed to investigate the MLT region since it provides a high horizontal × vertical resolution of ~110 km × 1.1 km, which is sufficient for the investigations performed in this paper.

The global ionization rates associated with protons, electrons, and alpha particles are provided by the 3-D atmospheric ionization module Osnabrück (AIMOS) version 1.6 [*Wissing and Kallenrode*, 2009]. The AIMOS model is based on a pair of Polar-orbiting Operational Environmental Satellites (POES) and one geostationary (GOES). It is therefore restricted to the measured energy spectra provided by the respective instruments, ranging from 154 eV to 500 MeV for protons, 154 eV to 300 keV for electrons, and 4 MeV to 500 MeV for alpha particles. Contamination of the electron channels (0.03–0.1 MeV and 0.1–0.3 MeV) was taken into account by excluding these channels from further analysis when the respective omnidirectional proton channel (165–

500 MeV) measures more than two counts (no unit available). Thus, electrons during the main phase of a solar proton event (SPE) and inside the South Atlantic Anomaly are not considered. The observed particle fluxes are converted to 2-hourly 3-D ion pair production rates in the atmosphere. The temporal resolution of AIMOS is limited to the model sampling of 2 h. Thus substorms and other short-term features cannot be captured in AIMOS. But since substorms are a common feature in the database, the temporal resolution of AIMOS will present a long-term average. The smallest theoretical horizontal resolution is defined by the grid of $3.6 \times 3.6°$ and was applied inside the auroral oval. Consequently, both temporal and spatial resolution of AIMOS is sufficient for these analyses.

Including the AIMOS ionization rates into the 3dCTM leads to formation of NO_x and HO_x per created ion pair. The underlying parameterization of NO_x considers various ionic and neutral reactions, depending on the atmospheric background state [*Nieder et al*., 2014]. The corresponding parameterization for HO_x and O production are based on the results reported by *Solomon et al.* [1981] and *Porter et al.* [1976].

The spin-up of the 3dCTM simulations was done in a dual stage process. First, a multidecadal run of the 2-D version of the 3dCTM [*Sinnhuber et al*., 2003] was carried out in order to find an approximate trace gas distribution on a latitude-altitude grid. The results of this model run were used as initial conditions for a subsequent dry run with the 3dCTM itself, leading to a well-mixed trace gas distribution after ~five model years. The corresponding total amount of the trace gas does not necessarily agree with respective observations. Consequently, the simulated total atmospheric amounts of the trace gases were individually scaled to match the measurements, while keeping the obtained spatial trace gas distribution of the 3dCTM. The resulting scaled trace gas distributions were eventually used as the initial conditions of the 3dCTM simulation. Six runs were carried out with the 3dCTM with different particle and solar spectral forcing (Table 1). The model runs are restricted by the availability of AIMOS and LIMA data to the period from January 2002 to May 2010.

The first set of simulations was carried out under constant solar minimum conditions ($F_{10.7} \sim 70 \times 10^{22}\,\mathrm{W\,m^{-2}\,Hz^{-1}}$) to exclude trace gas variations related to solar variability. The first simulation of this set did not include any particle effects and works as the reference (Base) scenario. The second run (PP run) considered ionization due to protons, electrons, and alpha particles. A third run (PP + PI run) additionally considered photoionization. The impact of photoionization was determined by using a Lambert-Beer absorption law that is dependent on the respective solar zenith angle. The variable spectral distribution was parameterized as suggested in *Solomon and Qian* [2005]. Subsequent chemical changes consider the atmospheric background state and were parameterized as described in *Nieder et al.* [2014]. To account for possible influence of solar variability, these three runs were also performed with an underlying varying solar spectrum [*Lean et al*., 2005], and the respective runs are referred to Base + F, PP + F, and PP + F + PI run. These simulations were used for a direct comparison of the 3dCTM results with actual observations, but they only cover the period from January 2002 to August 2008 due to missing solar data afterward.

2.2. Data and Method

The daily means from the 3dCTM of the investigated trace gases (OH, NO, and O_3) and the AIMOS ionization rates were grouped in daily nighttime (solar zenith angle $>96°$) and daily daytime means (solar zenith angle $<88°$), subsequently calculating nighttime and daytime mean zonal means which cover 55°–75° geomagnetic latitudes. The algorithm was individually applied for both the Northern Hemisphere (NH) and Southern Hemisphere (SH) while separately considering summer and winter season, defined by equinox. The geomagnetic latitudes were derived by approximating the Earth's magnetic field as a symmetrical dipole field. Furthermore, a wandering magnetic pole was also considered based on results of the international geomagnetic reference field model (version 10) [*Maus et al*., 2005]. Note that the disturbed patterns of the Earth's

Table 1. Summary of Performed Model Simulations[a]

Main Characteristics	No Particles or Photoionization	Included Particles	Included Particles and Photoionization
Constant solar spectrum; simulations from January 2002 to May 2010	Base run	PP run	PP + PI run
Varying solar spectrum; simulations from January 2002 to August 2008	Base + F run	PP + F run	PP + F + PI run

[a]Names of the individual 3-D chemistry and transport model simulations under constant and varying solar spectrum as well as relevant specifications.

magnetic field in the SH are not taken into account by this dipole field. The ionization rates provided by AIMOS indirectly consider the real Earth's magnetic field, because they are derived from satellite measurements. Thus, AIMOS and consequently the 3dCTM are based on the real Earth's magnetic field, as it is also true for observations. Therefore, the approximation of the Earth's magnetic field as a symmetrical dipole field does not play a crucial role for the validation of the 3dCTM, because the calculated geomagnetic latitudes cut out the same spatial region in both 3dCTM and observations.

Additionally, the influence of large solar proton events (SPEs) was excluded by removing days from the time series when the respective >10 MeV proton flux measured by GOES exceeds the commonly used threshold of 10 protons $cm^{-2}\,s^{-1}\,sr^{-1}$. The impact of SPEs was not considered due to their sporadic occurrence and different underlying source mechanism. Since the SPE date marks only the peak of the particle flux and it takes a few days for the trace gases to recover, 1 day before the start of the SPE and 5 days after the end of the SPE were also excluded. In case of O_3 the period was extended to 10 days. These limits were empirically derived and are based on observations presented by *Damiani et al.* [2008]. Finally, the trace gas amplitude as a function of day (d) and altitude (z) was calculated (equation (1)), representing relative deviations from the trace gas background (=27 day running mean). The factor 100% was added for more handy values.

$$\text{trace gas}(d,\ z) = \frac{\text{trace gas}(d,\ z) - 27\ \text{day running trace gas mean}(d,\ z)}{27\ \text{day running trace gas mean}(d,\ z)} \cdot 100\% \tag{1}$$

The geomagnetic *Ap* index (*Ap*) is derived from magnetometer measurements located at 13 ground-based observatories between 46° and 63° geomagnetic latitudes. However, variations in the magnetometer observations can have different sources, and *Ap* does not provide any information about the origin of the disturbances and the particle fluxes. However, *Ap* is still a suitable proxy to estimate global geomagnetic disturbances in the ionosphere and magnetosphere. Consequently, *Ap* was used here as an indicator of the probability of particle precipitation that reach the MLT region. Based on 3-hourly *ap* means, daily *Ap* means from 12 UT to 12 UT of the next day were calculated to match the model output at 00 UT. It should be noted that the auroral electrojet index (*Ae*) would have been more suitable for this study since this index explicitly focuses on the auroral latitudes investigated here. There is also the possibility to use AIMOS ionization rates which directly provide the particle forcing. However, *Ap* is the commonly used index for geomagnetic activity, which is used here for direct comparisons with the observations reported in literature.

The applied superposed epoch analysis (SEA) is a useful statistical tool to extract a periodic or nonperiodic signal from background variability, which is superposed by other signals of the same time scale. It has been shown that the SEA is suitable to analyze a signal with a varying phase and frequency, like the 27 day signal associated with solar wind variations [e.g., *Friederich et al.*, 2014; *Hendrickx et al.*, 2015]. The method is based on sorting the data set with respect to previously defined key events and comparing the averages of all time intervals (periods) around these key events. Based on the time series of *Ap*, the average (27 day *Ap* mean) and the standard deviation $\sigma(Ap)$ were calculated for a running 27 day window centered at day d. Subsequently, a day was defined as an event day if equation (2) is fulfilled:

$$[Ap(d) - 27\ \text{running}\ Ap\ \text{mean}(d)] > \sigma[Ap(d)]. \tag{2}$$

In order to analyze the 27 day solar rotational signal, all ±30 day periods (epochs) around every event day were arithmetically averaged (superposed) to obtain the SEA signal. The threshold for the key events (equation (2)) was empirically determined and was chosen to ensure at least 50 events in each hemisphere-season interval to increase statistical significance. This criterion results in 183 (201) events during boreal summer (winter) for Base, PP, and PP + PI runs. The period covered by the Base + F run, PP + F run, and PP + F + PI run is shorter and amounts to only 150 events. Note that the applied criterion permits consecutive days as event days. Therefore, only about 2/3 of these events are associated with single events if consecutive event days are regarded as one event. Furthermore, small *Ap* variations during geomagnetic quiet times can be considered as events since the corresponding standard deviation is also small. These events only contribute to a lesser degree to the overall SEA signal. But including these events yields the advantage that the events are approximately uniformly distributed throughout the entire time interval from 2002 to 2010. Consequently, the SEA signal represents an average of the considered period.

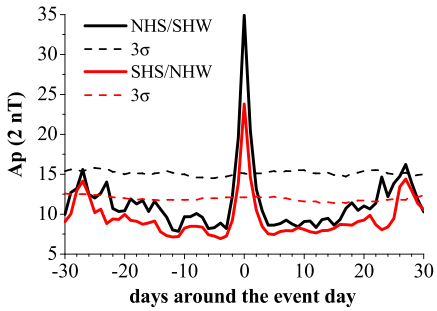

Figure 1. Superposed epoch analysis results for the *Ap* index from January 2002 to May 2010 during Northern Hemisphere summer (NHS) and Southern Hemisphere winter (SHW) as well as Southern Hemisphere summer (SHS) and Northern Hemisphere winter (NHW), showing ±30 days around the event day (day 0).

The significance of *Ap*, AIMOS ionization rates, and the trace gas amplitudes of the individual model runs was estimated using a Monte Carlo approach [*Laken and Calogovic*, 2013]. This method is based on a large sample of random (pseudo) epochs to derive the underlying (empirical) probability density, including potential autocorrelation of the data. In this case, 150 randomly chosen events were used to calculate a pseudo SEA signal. This calculation was repeated 10,000 times, eventually resulting in a background probability density for each pseudo SEA day. The 99% significance level shown in this paper is based the 0.005 and 0.995 quantiles of these distributions for each day. Thus, the 99% significance level represents the internal variability of the data set.

3. Results and Discussion

The SEA results for *Ap* during Northern Hemisphere summer (NHS) and Southern Hemisphere winter (SHW) as well as in Southern Hemisphere summer (SHS) and Northern Hemisphere winter (NHW) are displayed in Figure 1, showing three local maxima at the event day and at day ±27. The signatures are marked by a major peak at day 0 with *Ap* values of about 35×2 nT (24×2 nT) during boreal summer (winter), while two further maxima of about $14–16 \times 2$ nT are located at day ±27. While the major maximum results from the construction of the SEA, this does not hold for the secondary peaks, a clear indication of a periodic signal. All maxima exceed at least the 99% significance level, making it likely that the observed 27 day signature is a real feature.

The reason for the dominating maximum at the event day compared to the secondary peaks is caused by the influence of nonperiodic events like coronal mass ejections which only contribute to the signal at the event day and not to the minor peaks. In contrast, the recurrent CIRs affect all three maxima in a similar way. Thus, only variations close to the secondary maxima are solely related to the 27 day signal. It should be further considered that the three maxima are not limited to a single day because successive days can be classified as individual events. Note that the presented 27 day signature is associated with particle precipitation and not related to solar ultra violet (UV) radiation. Both particles and solar radiation show a 27 day signature, but the 27 day signal in solar UV radiation shows a different shape and a varying phase relation [*Fytterer et al.*, 2015].

The SEA results of AIMOS ionization rates associated with electrons (hereafter referred to as ionization rates) during SHW are displayed in Figure 2. Their main patters hold for each hemisphere-season interval but are strongest during SHW which is consistent to *Ap*. A distinct 27 day signature is apparent that is in phase with *Ap*. The largest response occurs at 115 km, reaching values $>1800\,\mathrm{cm^{-3}\,s^{-1}}$ at day 0 and $>1200\,\mathrm{cm^{-3}\,s^{-1}}$ at day ±27. Furthermore, the major direct impact (ionization rates $>100\,\mathrm{cm^{-3}\,s^{-1}}$) of electrons is limited to the altitude region above 80–85 km, where all three peaks generally exceed the 99% significance level. The results also show ionization at altitudes <70 km, which does not originate from particle ionization because only electrons with energy levels <300 keV are included in AIMOS. The ionization in this region is generated by bremsstrahlung from electrons that are stopped at altitudes above 70 km. The ionization associated with alpha particles is usually 2 to 3 orders of magnitude lower compared to electrons. Furthermore, the overall impact of protons is substantially weakened due to the exclusion of SPEs, and consequently, ionization rates of both alpha particles and protons are not shown here. It should be pointed out that it is not recommended to scale the maxima of the ionization rates by respective maxima of *Ap* since their relation is probably nonlinear.

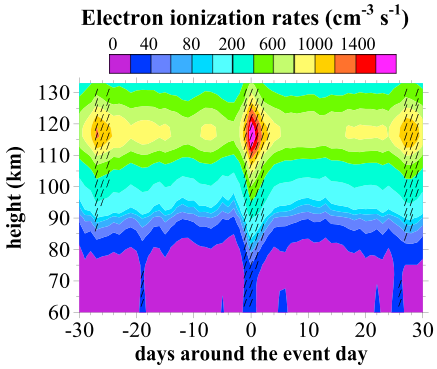

Figure 2. Superposed epoch analysis results of the ionization rates ($cm^{-3}\,s^{-1}$) associated with electrons during SHW. Values above 99% significance level are shaded (slash). Note the nonlinear scaling.

3.1. Simulated Particle Precipitation Impact on Atmospheric Trace Gases

The SEA amplitudes of the Base run were subtracted from the respective SEA amplitudes of the PP run. This ensures that the influence of dynamical induced variations of the atmospheric background is minimized. Note that only these particle-induced trace gas amplitudes are considered in this chapter. The impact of the variations of the atmospheric background on the particle precipitation patterns in the trace gases is discussed in sections 3.3 and 3.4. The applied error estimation fails to provide reasonable results here, because the background variability of the model is eliminated by subtracting the amplitudes of the Base run from the amplitudes of the PP run. Thus, no estimation of the significance was added in this section. Obviously, not all trace gas differences shown can be related to particle impacts and might also originate from numerical noise. But the smallest variations considered here are trace gas amplitudes of about 1% over a background of ~1 ppb, which is equivalent to variations of about 10^{-11}. These variations are several orders of magnitude larger than the random errors (numerical noise) of the 3dCTM results (~10^{-20}). Thus, strong signals that resemble shape and occurrence time of the signal in *Ap* are very likely caused by particle precipitation. However, it should be pointed out that only trace gas variations up to the magnitude of the secondary maxima close to the day ±27 are solely related to the 27 day signal, while the maxima at the event day partly originate from nonperiodic events (see Figure 1 and description).

3.1.1. NO

The NO amplitudes are displayed in Figure 3 but only for the NH since their main features are similar in both hemispheres. Daytime summer NO patterns (Figure 3a) show a distinct 27 day signal between 80 km and 110 km. Maximum amplitudes are found at 90–95 km and last up to 3–4 days, reaching ~120% at the event day and about 50% at day ±27. The NO response is in phase with *Ap* and ionization rates at heights >105 km but usually delayed by +1 day at altitudes below. Also considering that maximum ionization rates are found at 115 km, it is reasonable to assume that the upper part of the NO signal is directly caused by ionization while the lower response evolves from an accumulation effect of NO. The nighttime NO patterns during NHW (Figure 3b) also reveal a well-pronounced 27 day signal. The instant response of maximum NO enhancement at day 0 is restricted to altitudes >110–120 km but becomes delayed by a few days at lower altitudes. Here the NO amplitudes form a slope between 75 km and 95 km that is supposedly caused by downward transport in combination with the chemical NO lifetime of a few days. The largest amplitudes are located between 110 km and 115 km (~60% at day 0 and 30% at day ±27), again overlapping with the occurrence altitude of maximum ionization rates. Therefore, winter amplitudes occur at higher altitudes and are weaker compared to summer. These interseasonal differences are primarily attributed to the substantially higher-NO background in winter at altitudes below 120 km (Figure 4), damping the winter amplitudes compared to their respective summer values.

In order to investigate the temporal evolution of the NO enhancements induced by particle precipitation (not the 27 day response) after the event in more detail, height profiles of the NO amplitudes from day 0 to +5 for NH are displayed in Figure 5, left column, while the respective differences to the SH are shown in the right column. The formation of NO during NHS (Figure 5a) is marked by a broad maximum at day 0 (80–85%), which is narrowed and intensified to a single peak after 1 day. This vertical pattern is generally conserved on the following days while the respective amplitudes become weaker and eventually vanish into the background at day +5. Additionally, the entire structure descends down by a few kilometers, which is less likely caused by transport but rather due to the decreasing NO lifetime at higher altitudes. Larger inter-hemispheric differences occur below 90 km (Figure 5b) because the NO response in the SH vanishes faster into the background. Therefore, largest NO amplitudes are found at day +1 although the NO lifetime is shorter than 1 day

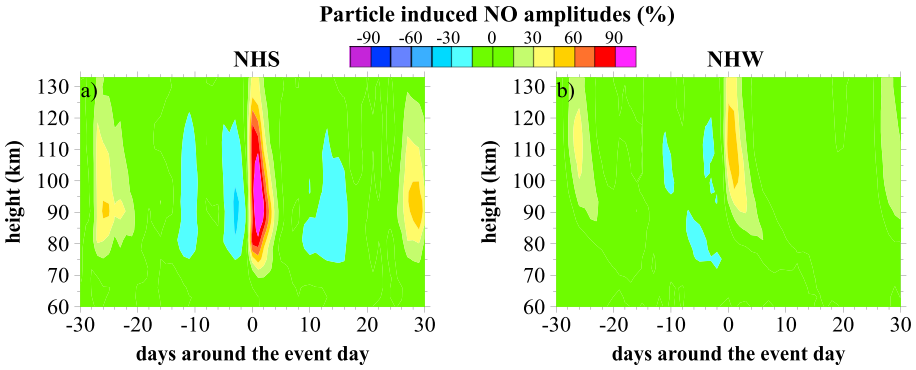

Figure 3. Amplitudes of NO in the Northern Hemisphere during (a) daytime summer and (b) nighttime winter solely associated with particle precipitation (PP run − Base run). The amplitudes were calculated from a superposed epoch analysis applied to the 3dCTM simulations from January 2002 to May 2010 at 55°–75° geomagnetic latitudes.

during summer. The reason might be that the 3dCTM only provides a snapshot of the atmosphere at 00 UT and not a real daily mean, which can shift the maximum NO enhancement by half a day.

The nighttime simulations during NHW (Figure 5c) show that particle-induced NO production occurs as a single peak without temporal delay compared to *Ap*, which maximizes at day +1. The shape of the vertical profile is unchanged in the following four days, but the maximum NO amplitude propagates downward from 110 km to 85 km and decreases below 20%. In contrast to summer, the downward movement is caused by large-scale transport pattern and not by photochemistry. Substantial interhemispheric differences are only found with respect to their amplitude magnitude. The NHW NO amplitude shows instant growth at the event day, while the respective SHW amplitude rises in two steps at day 0 and day +1 (Figure 5d). Furthermore, the SHW amplitude maximum is slightly smaller than in NHW, although the reversed behavior is visible in *Ap* and ionization rates. Consequently, NO formation is suggested to work differently in both hemispheres. The applied NO parameterization considers the different atmospheric background conditions such as the abundance of O^3P, which is substantially higher in NHW than in the SHW and compensates the stronger *Ap* and ionization rates. The occurrence of the maximum at day +1 in each hemisphere and season is probably caused by an accumulation effect because particle precipitation is usually not cut off after 1 day and the NO chemical lifetime is generally about at least 1 day.

3.1.2. OH and O_3

The simulated particle impact on OH and O_3 during SHW is displayed in Figure 6, representing the main general features in each hemisphere-season interval while their response is strongest in SHW. In OH (Figure 6a), a 27 day signal is weakly visible and centered at the event day. Maximum amplitudes are located at the event day at 70–75 km (+11%), and a further peak is found at 85 km (+9%), both lasting for 1–2 days. However, variations solely associated with the 27 day signal are only about +4%. The 27 day response in O_3 (Figure 6b) is indicated between 70 km and 80 km (−2%) and in phase with *Ap*. The O_3 depletion at the event day extends from 65 to 90 km and maximizes at 70–75 km (−8%). Therefore, the O_3 response overlaps with the altitude of the maximum OH amplitude, supporting a direct relation. The O_3 amplitudes at day +1 are occasionally of similar magnitude as at the event day, indicating that OH induced O_3 depletion is slightly delayed to particle induced OH production. Nevertheless, these results suggest that the OH-O_3 chemistry implemented in the 3dCTM works reasonable.

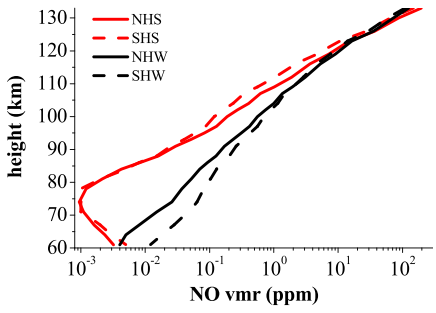

Figure 4. Vertical profiles of NO background based on the 3dCTM PP run from January 2002 to May 2010 at 55°–75° geomagnetic latitudes.

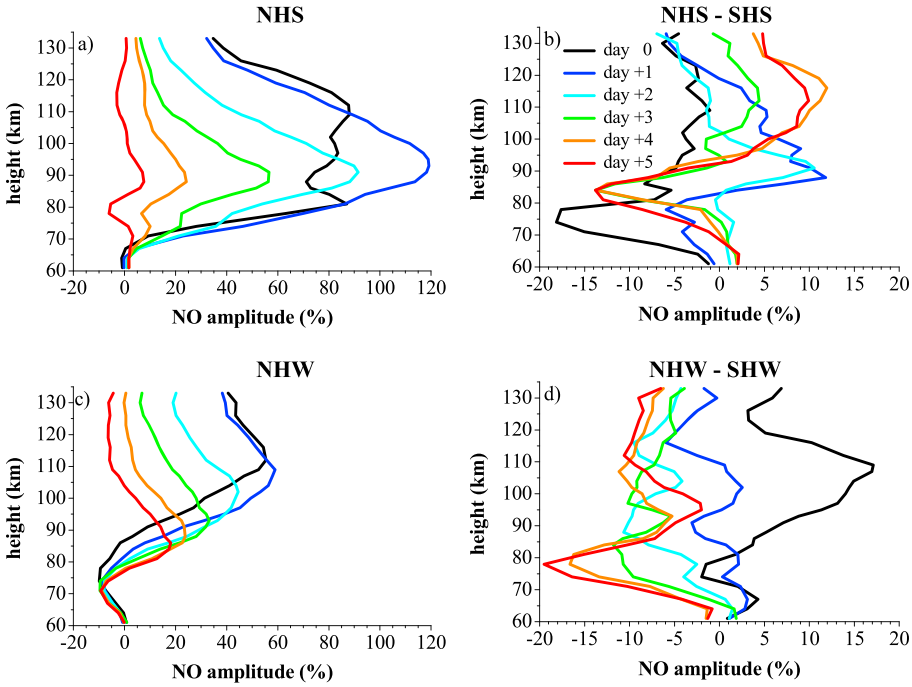

Figure 5. Height profiles of the NO amplitudes from the superposed epoch analysis day 0 to day +5 solely associated with particle precipitation in the Northern Hemisphere during (a, b) daytime summer and (c, d) nighttime winter. Figures 5b and 5d show the differences to the respective Southern Hemisphere amplitudes.

Both OH and O_3 amplitudes reveal large interseasonal variations (not shown here) in the SH due to their negligible response in summer (<±1%). The corresponding values in the NH vary about 1 to 3%, while the OH enhancement and O_3 loss are more pronounced in winter. The generally weaker response of both species in summer is caused by increased influence of solar UV radiation. This leads to higher photolysis rates of water vapor, which plays the key role in OH production and damps the particle impact during summer. Additionally, O_3 quickly recovers in less than 1 day during summer even after the strong SPE in January 2005 [*Damiani et al.*, 2006]. The reason for the weak interseasonal variability in the NH is probably that particle precipitation and solar UV impact incoherently superpose.

3.2. Impact of Solar Spectrum Variability

Comparisons of the SEA results of the simulations with and without the varying solar spectrum from January 2002 to August 2008 (not shown here) imply that the main isolated particle precipitation patterns in the trace

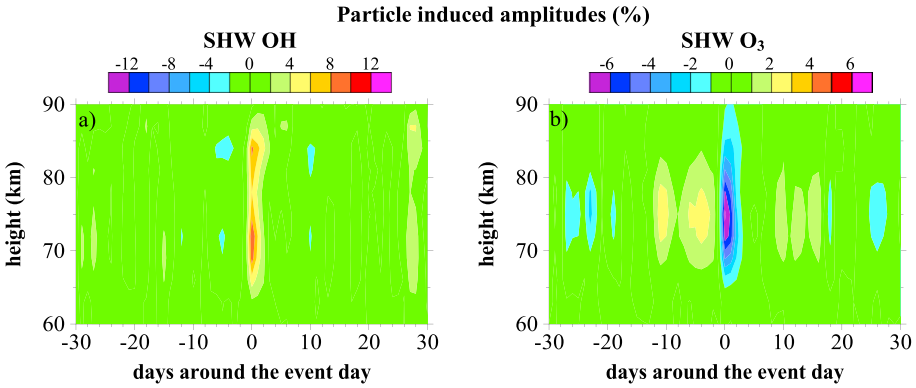

Figure 6. Nighttime amplitudes in Southern Hemisphere winter for (a) OH and (b) O_3 due to particle precipitation (PP run – Base run), derived from a superposed epoch analysis of the 3dCTM simulations from January 2002 to May 2010 at 55°–75° geomagnetic latitudes.

gases are generally conserved. However, the amplitude magnitude was occasionally affected, which is partly due to modifications of the trace gas background. In detail, solar variability causes an increase of NO amplitudes in summer by the factor of 1.1 or about 10%. A different response of both OH and O_3 is noticeable during winter, when their amplitudes are amplified by the factor of 1.1 and 1.05, respectively. An influence in summer was not found due to their generally small amplitudes. Therefore, the model results indicate that the impact of the solar cycle on particle precipitation pattern in atmospheric species cannot be completely neglected, even if the period considered here does not cover the entire 11 year solar cycle. A possible impact of photoionization was also investigated for both the simulations with the varying and with the constant solar spectrum, confirming that photoionization only plays a negligible role. The reason is that photoionization indeed produces additional ions. However, further neutral compounds can be also formed due to dissociative photoionization that leads to the depletion of previously formed radicals (e.g., $N(^4S) + NO \rightarrow N_2 + O$).

3.3. Comparison to Observations From Literature

The 3dCTM PP + F run is used in this section for direct comparisons with observations. Note that the corresponding atmospheric background (Base + F run) was not subtracted. Therefore, in contrast to section 3.1, the PP + F run does additionally include differences due to variations of the atmospheric background. The PP + F simulation also considers trace gas changes caused by the 11 year solar cycle signal. The variability of the atmospheric background is associated with small-scale dynamics and further analyzed in section 3.4.

3.3.1. O_3 and Its Relation to OH

Considering altitude and time of the isolated particle precipitation impact on NO, OH, and O_3 presented in section 3.1, it is more likely that OH or HO_x species are the main cause of short-term O_3 depletion rather than NO. This is supported by model studies and satellite observations presented by *Jackman et al.* [2014]. The 3dCTM output from the PP + F run of nighttime OH and O_3 during NHW and SHW is shown in Figure 7. The OH response in NHW (Figure 7a) indicates a 27 day signature in phase with *Ap* and ionization rates, which becomes more apparent at ~85 km. Here maximum amplitudes of about +6% are found at the event day. In the SHW (Figure 7b), the 27 day signal is weakly seen between 70 km and 85 km and marked by two maxima at day 0 at ~70 km (+14%) ~85 km (+10%), both exceeding the 99% significance level. In both hemispheres, OH enhancements related to the 27 day signal are about 2–4%.

The magnitude of OH amplitudes in both hemispheres is consistent with *Ap* and ionization rates from January 2002 to August 2008 which are generally similar to the results presented in Figures 1 and 2. The interhemispheric differences might also be affected by temperature, but the impact is hard to identify since temperature influences the whole chemistry. Furthermore, the impact is probably weak compared to the changes induced by particle precipitation and variations of the background atmosphere due to small-scale dynamics. Therefore, no attempt was made to analyze a possible temperature induced OH variations.

The corresponding O_3 response in NHW (Figure 7c) shows no apparent 27 day signature related to particle precipitation. The structures are broader and less resemble the features in *Ap* and ionization rates. In contrast, the O_3 amplitudes in SHW (Figure 7d) at least indicate a 27 day signature between 70 km and 80 km, but only the amplitudes close to day 0 exceed the 99% significance level. Therefore, these results should be treated with care. The largest amplitudes are located at ~75 km, reaching values up to −12% at days 0–1, while the response in NHW is slightly stronger (−14%) and shifted to day +2.

The 27 day response of nighttime OH (O_3) associated with *Ap* in Aura/Microwave Limb Sounder (MLS) satellite observations from 2004 to 2009 (2004 to 2014) between 60 km and 81 km (60 km and 75 km) at 55°–75° geomagnetic latitude was reported by *Fytterer et al.* [2015]. Their results in NHW show that the observed OH amplitudes are considerably stronger than in the 3dCTM, while the general patterns are similar. These differences are mainly caused by the nearly 1 order of magnitude higher simulated OH background compared to the MLS observation (Figure 8a). The overestimation of the respective O_3 model amplitude magnitude is also related to the lower 3dCTM O_3 background (Figure 8b). However, this does not explain the missing agreement with respect to the shape of the response, which should still resemble the signature in *Ap*. Since the O_3 amplitudes solely associated with particle impacts indicated a 27 day signal (see Figure 6b and section 3), these huge differences are therefore attributed to dynamical induced variations of the atmospheric background. Due to the longer life time of O_3, the O_3 amplitudes might be more affected than the response in OH. To have a closer look into this issue, a major sudden stratospheric warming (SSW) was

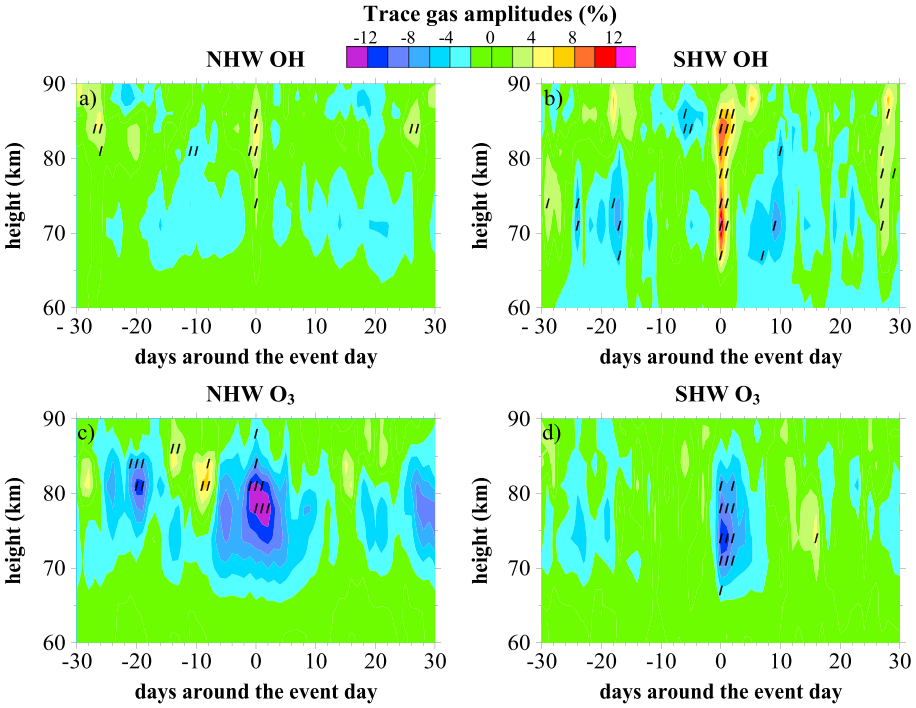

Figure 7. Nighttime winter amplitudes of (a) NHW OH, (b) SHW OH, (c) NHW O_3, and (d) SHW O_3 between 55° and 75° geomagnetic latitudes, derived from the 3dCTM PP + F run from January 2002 to August 2008. Shaded areas (slash) show amplitudes above 99% significance level.

defined by the reversal of the zonal wind at 10 hPa [*Andrews et al.*, 1987, chap. 6.1], based on the zonal mean wind at 50°–80°N. In the next step, periods of ±40 days around major SSWs were excluded. The threshold of 40 days was empirically determined in order to avoid an influence on the 27 day running means and takes the downward propagation of the wind reversal with time [e.g., *Manney et al.*, 2009] into account. However, in agreement with results reported by *Hendrickx et al.* [2015] the general patterns were conserved while changes in the amplitude magnitude can be attributed to the different number of events.

The results reported by *Fytterer et al.* [2015] support that the peak in OH (O_3) at ~70 km (75 km) in SHW is captured by the 3dCTM, with respect to occurrence time, duration, and the amplitude magnitude. It should be noted that the OH model background is substantially higher than in the observations (Figure 8a), but this damping effect might by overcompensated by the stronger *Ap* signal during the period of the 3dCTM simulations (39 × 2 nT) compared to the measurement time interval (20 × 2 nT). The occurrence of the measured OH maximum at slightly higher altitudes (75 km) might be attributed to the coarser vertical resolution of the observations. The simulated O_3 amplitude is approximately overestimated by the factor of 2. However,

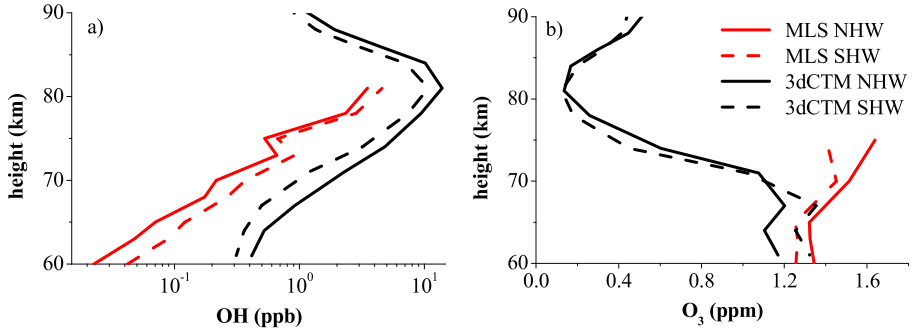

Figure 8. Vertical profiles of (a) OH and (b) O_3 background based on the 3dCTM PP + F run from January 2002 to August 2008. The Aura/MLS measurements are adapted from *Fytterer et al.* [2015].

the O_3 model background is only about 1/3 of the corresponding Aura/MLS O_3 background (Figure 8b). Taking this into account, the O_3 model amplitude at day 0 will be damped to −4%, and the remaining differences to the observations can be attributed to measurement errors and the different time intervals. It should be noted that the model O_3 background profiles presented here are supported by the results of several instruments reported by *Smith et al.* [2013, Figure 8]. Thus, the 3dCTM O_3 background at ~75 km might be only too low compared to Aura/MLS observations.

Apart from the previously examined 27 day signal, this section provides a closer look at the relationship between geomagnetic activity, OH, and O_3 during winter. All events were sorted from weak to strong, according to the events magnitude ($\Delta Ap = Ap$ at the day − 27 day running Ap mean), and eventually grouped into 16 overlapping intervals (event groups) of approximately equal number of events (~40). Finally, the SEA was individually carried out for each event group and trace gas. Note that absolute trace gas anomalies (= trace gas at the day − 27 day running trace gas mean) were considered here, since O_3 depletion depends on the absolute amount of OH and O_3. The OH and O_3 anomalies of the maximum at ~75 km close to day 0 are plotted as a function of ΔAp in Figure 9 and are compared to the identically calculated anomalies of Aura/MLS satellite observations from 2004 to 2009 (OH) and from 2004 to 2014 (O_3) [*Fytterer et al.*, 2015].

The main relative pattern of the measured OH is reproduced by the 3dCTM in the NHW (Figure 9a). The anomalies show nearly no response for weak geomagnetic events, and model anomalies are partly negative, implying that the particle impact is superposed by other effects such as dynamical variability of the background atmosphere. The sharp anomaly increase at $\Delta Ap \sim 10–15 \times 2$ nT is substantially more pronounced in the simulations which show a rise by a factor of about 7, but the observed anomalies only double. While only indicated by the measurements, the 3dCTM suggests that OH formations slows down for stronger geomagnetic activity ($\Delta Ap \sim 15–35 \times 2$ nT). In SHW (Figure 9b), the relative behavior of the modeled anomalies is also in agreement with the measurements, including a weak particle precipitation impact on OH for $\Delta Ap < 21 \times 2$ nT and a large growth for stronger events. Similar to NHW, the OH enhancement slows down for moderate events, but the simulations indicate a further rise between $\Delta Ap \sim 45 \times 2$ nT and $\Delta Ap \sim 70 \times 2$ nT. Both 3dCTM and observation suggest that the response of OH enhancement to ΔAp is delayed in SHW compared to NHW. The reason for this might be that the Earth's magnetic field was approximated as a symmetrical dipole field. Consequently, the calculated and real geomagnetic latitudes agree less in the SH, including the location of the auroral latitudes.

As presented in Figures 9a and 9b, the 3dCTM overestimates the OH anomalies in both winter hemispheres approximately by a factor of 5 and potential reasons are discussed below. Nevertheless, the main relative patterns are qualitatively reproduced by the 3dCTM. This includes the indicated threshold in geomagnetic activity, which has to be exceeded to trigger OH formation. Furthermore, the slowdown of OH formation is also supported, and both characteristics are already discussed in *Fytterer et al.* [2015].

In the model, the OH or HO_x production is a linear interpolation of the ionization and geometric altitude based on *Solomon et al.* [1981, Figure 2]. Therefore, an offset of the ionization rates provided by AIMOS could cause an overestimation in OH anomalies. Such an offset in AIMOS is not known so far but cannot be ruled out. This becomes apparent by the comparison of electron densities derived from an AIMOS driven model and incoherent scatter measurements, at least indicating a systematic offset during high geomagnetic activity [*Wissing et al.*, 2011]. A further parameter influencing OH production is the abundance of H_2O, which is indirectly considered by the geometric altitude. In particular the heights between 70 km and 85 km are a crucial region because of the large vertical gradient of water vapor. But the dependence of water vapor is considered using only one standard profile based on daytime polar summer conditions. This overestimates H_2O during polar winter because the downwelling of H_2O-deficient air is not considered in model OH production, consequently overestimating HO_x production in the model in polar winter.

Additionally, an incorrect chemical reaction constant could also lead to the simulated systematic overestimation. But identifying such constants requires an extended sensitivity study, which is beyond the scope of this paper. An offset of the dynamics in general can possibly result in an overestimation of OH. This is reasonable because the impact of dynamics is less represented by the LIMA model during winter while the time constant of the horizontal transport is only about a few days [*Brasseur and Solomon*, 2005, Figure 5.27]. The analysis displayed in Figures 9a and 9b were repeated for OH anomalies in winter but

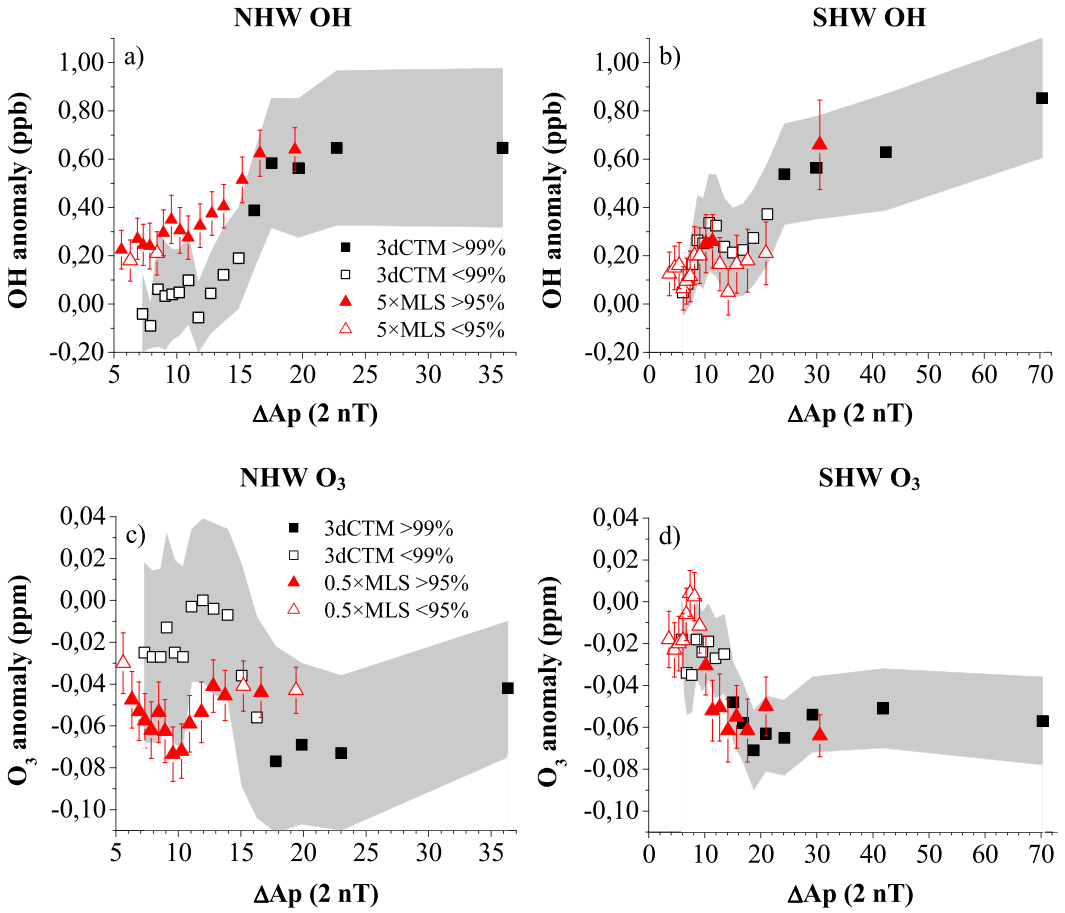

Figure 9. Absolute anomalies of (a) NHW OH, (b) SHW OH, (c) NHW O_3, and (d) SHW O_3 as a function of the event magnitude (ΔAp), derived from the maximum close to day 0 at 75 km of the superposed epoch analysis of the 3dCTM PP + F run from January 2002 to August 2008. Filled symbols show anomalies above the 99% significance level. The 1σ error of the anomalies is added as a shaded area (3dCTM) and as an error bar (Aura/MLS). The Aura/MLS observations are multiplied by the factor of 5 (OH) and by the factor of 0.5 (O_3) (adapted from *Fytterer et al.* [2015]). Note the different scaling for OH and O_3.

for the Base run (not shown here). The results generally show OH variations in the range of 0.0–0.3 ppb but reveal no dependence of ΔAp. Thus, variations of the atmospheric background cannot be the cause of the overestimation.

Comparisons between Aura/MLS measurements and 3dCTM output for O_3 (Figures 9c and 9d) show that the anomalies are generally underestimated by the model by a factor of 2. However, the simulated relative pattern in NHW is similar to the observations but delayed with respect to ΔAp. Therefore, substantial O_3 depletion occurs in the model for $\Delta Ap > 15 \times 2$ nT, while the measured O_3 loss already takes place for $\Delta Ap < 10 \times 2$ nT. The O_3 depletion is suggested to be damped for larger ΔAp. The relative variability of the O_3 anomalies in SHW is also qualitatively captured by the 3dCTM, including the strong rise for weak events ($\Delta Ap < 15 \times 2$ nT) and the saturation effect for stronger geomagnetic activity. The latter feature is seen in the 3dCTM and the observations and additionally visible in both hemispheres. The reason might be that mesospheric O_3 depletion depends on both the abundance of OH and O_3. Thus, if O_3 is rapidly depleted, it slows down the reactions rates of the involved catalytic cycles. This causes a less efficient O_3 loss for relatively weak OH enhancement and has already been discussed in *Fytterer et al.* [2015]. Therefore, the model simulations suggest a nonlinear relation between OH and O_3 during SHW, matching the corresponding measurements.

Usually, larger OH enhancements are expected to correspond with stronger O_3 loss. That seems to be in conflict with the presented overestimation of OH anomalies by the 3dCTM, while the respective O_3 depletion is

underestimated. A possible reason might be the substantially lower O_3 model background at ~75 km, which is only of about 1/3 of the measurements (Figure 8b). Consequently, this lower O_3 background limits the OH-induced catalytic O_3 loss because the O_3 depletion by OH depends on both the abundance of OH and O_3. Note that the lower O_3 background only leads to weaker absolute O_3 variations (anomalies), as they are considered in Figure 9. In contrast, relative variations with respect to the O_3 background (amplitudes) are amplified by the lower O_3 background, as shown in Figure 7d and the corresponding discussion.

Furthermore, mesospheric O_3 loss is primarily attributed to H and not OH [e.g., *Jackman et al.*, 2014]. Additionally, OH only accounts for 1/3 of HO_x at ~75 km in the 3dCTM, while the ratio H/HO_x is approximately 2/3. Consequently, OH might not be a suitable proxy for HO_x at 75 km [*Fytterer et al.*, 2015]. To analyze the relation between HO_x and its individual components, the SEA was separately carried out for the 16 event groups and applied for HO_x, H, OH, and HO_2 from the PP + F run between 60 km and 90 km during winter. The linear correlation coefficients between HO_x anomalies at the event day and the respective anomalies of the individual HO_x compounds were calculated. The results ensured that OH is a reasonable indicator for HO_x in both hemispheres at altitudes $\leq$75 km ($r > 0.9$). Although a final conclusion cannot be drawn at this point, the underestimation of O_3 anomalies despite the overestimation of OH enhancement originates from a systematic error that is likely related to the lower O_3 model background compared to the measurements.

3.3.2. NO and Its Impact on O_3

The 3dCTM PP + F simulations of NO during SHS and SHW are displayed in Figure 10, also representing the main features in the NH. The NO amplitudes in SHS (Figure 10a) show a distinct 27 day signature at altitudes >70 km that usually exceeds the 99% significance level. The response is in phase with *Ap* at altitudes >110 km and is shifted by +1 day below. The largest amplitudes occur at 95 km at day +1 (>100%), while the secondary maxima are about 60–70%. The NO response in SHW (Figure 10b) is centered at day +1 and becomes more out of phase below 100 km due to downward transport. The strongest peaks are located at 110 km, reaching values of ~50% at the event day and about 20% at the secondary maxima. The results show negligible differences to the isolated particle impact on NO (see Figure 3), strongly indicating that geomagnetic activity is the major source of NO production in the MLT throughout the year.

The SEA was repeated for ENVISAT/Scanning Imaging Absorption Spectrometer for Atmospheric Chartography (SCIAMACHY) daily NO number density measurements from 2002 to 2012 at 55°–75° geomagnetic latitudes between 64 km and 84 km, similar to the results presented by *Sinnhuber et al.* [2016]. Only the pattern in polar summer could be analyzed since SCIAMACHY observations are based on limb scan measurements of the NO γ-bands, which are excited by photoabsorption. The results are displayed in Figure 11 and are qualitatively reproduced by the 3dCTM, including the amplitude magnitude, the phase of the 27 day signal, and the weak interhemispheric differences. The only striking disagreement is found in the vertical profiles of the three maxima which extend to 5 km lower altitudes in the observations. However, that is attributed to the limited energy range of AIMOS ionization rates used here, since the highest electron energy is 300 keV that approximately corresponds to an intrusion down to only ~70 km. Furthermore, 27 day signal is more pronounced in the simulations, which is consistent with the respective signal in *Ap*.

Hendrickx et al. [2015, Figure 5] performed a similar SEA for absolute daily NO anomalies derived from Aeronomy of Ice in the Mesosphere/Solar Occultation For Ice Experiment (AIM/SOFIE) satellite instrument measurements from 2007 to 2012 with respect to *Ae*. The observations cover 65°−85° geographic latitudes between 35 km and 130 km from November to February and from May to August, representing NHW and SHS and NHS and SHW, respectively. Their results resemble the model output with respect to shape and occurrence time of NO enhancement during summer. But the simulated NO amplitudes extend to lower altitudes (70 km), because relative deviations (amplitudes) were considered in our paper. The observations during winter agree that largest NO formation is found in the lower thermosphere 1–2 days after the event, lasting up to day +5. The measurements further support the downward transport of NO into the mesosphere. All these observed features occur about 1 day later than in the simulations. However, the major peak in *Ae* is centered at day 0 and day +1, while signal in *Ap* shown here dominates at the event day (see Figure 1).

In principle, NO_x could also contribute to O_3 depletion since HO_x formation is accompanied by NO_x enhancement [*Sinnhuber et al.*, 2012]. Further support of this proposal was reported by *Daae et al.* [2012] who observed mesospheric NO enhancement accompanied by O_3 depletion related to a moderate geomagnetic storm in late July 2009 in the SH. However, it was not completely ruled out that NO formation acts only as a

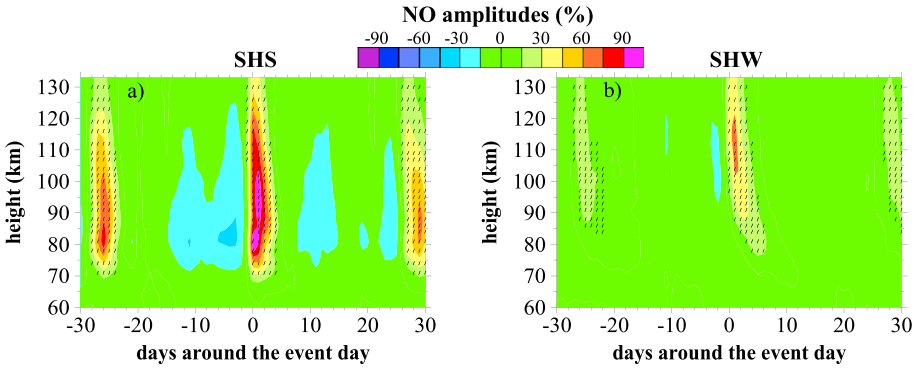

Figure 10. Amplitudes of NO during (a) SHS and (b) SHW between 55° and 75° geomagnetic latitudes, derived from the 3dCTM PP + F run from January 2002 to August 2008. Shaded areas (slash) show amplitudes above 99% significance level.

proxy for geomagnetic activity, while short-term O_3 loss is actually caused by HO_x species. Therefore, the time series of O_3, NO, and OH amplitudes from day 0 to day +10 between 70 km and 90 km were investigated. The analysis was limited to winter conditions because the NO signal coincides with the enhancement of background OH during summer, making their individual impacts on O_3 hard to distinguish. However, although the NO enhancement occasionally coincides with weaker O_3 depletion, the overall results do not further support that NO contributes to mesospheric O_3 loss. Thus, we strongly suggest that the NO enhancement observed by *Daae et al.* [2012] in SHW only overlaps in space and time with short-term O_3 loss due to the simultaneously produced HO_x which leads to catalytic O_3 destruction.

3.4. The Role of Dynamical Induced Variation of the Atmospheric Background

Since the results of the previous sections show a strong dynamical impact on the O_3 amplitudes, we analyzed energetic electron precipitation (EEP) events and the accompanied short-term O_3 variations reported in literature. Therefore, O_3 amplitudes with respect to the 7 day average prior to the EEP event were calculated to match the results reported by *Andersson et al.* [2014, Figures 2a–2c and supporting information Figure S1a]. Note that the observations are focused on 55°–65° geomagnetic latitudes, but the general impact associated with the different latitude bands should not change. The impact of dynamical induced variations of the atmospheric background on O_3 was excluded by subtracting the O_3 amplitudes of the Base + F run from the respective values of the PP + F run. Consequently, the differences between the results of the PP + F run and the (PP + F run − Base + F run) account for dynamical related variability.

The first considered EEP event started on 14 April 2006, and the O_3 loss in the SH simulated by the 3dCTM is shown in Figure 12a. At altitudes ~70–80 km, O_3 depletion up to nearly 30% is visible for 1–2 days after the event. The response additionally shows large O_3 enhancement before (+40%) and after (+90%) the event that extends down to 65 km. This is in qualitative agreement with the observations, including the magnitude and

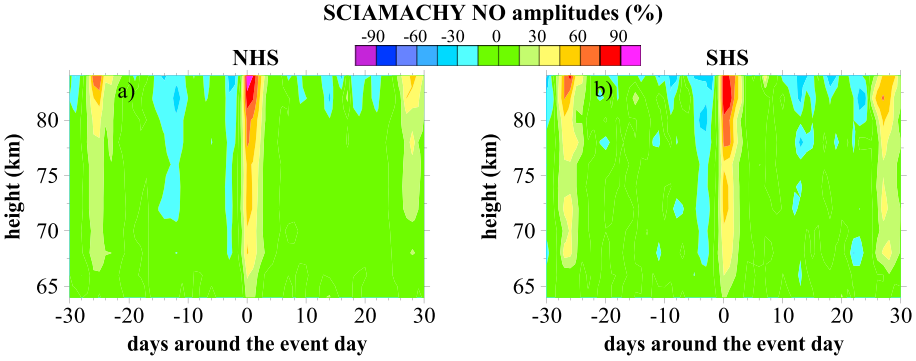

Figure 11. Amplitudes of daytime NO during (a) NHS and (b) SHS, derived by a superposed epoch analysis from ENVISAT/SCIAMACHY satellite instrument measurements from 2002 to 2012 at 55°–75° geomagnetic latitudes (adapted from *Sinnhuber et al.* [2016]).

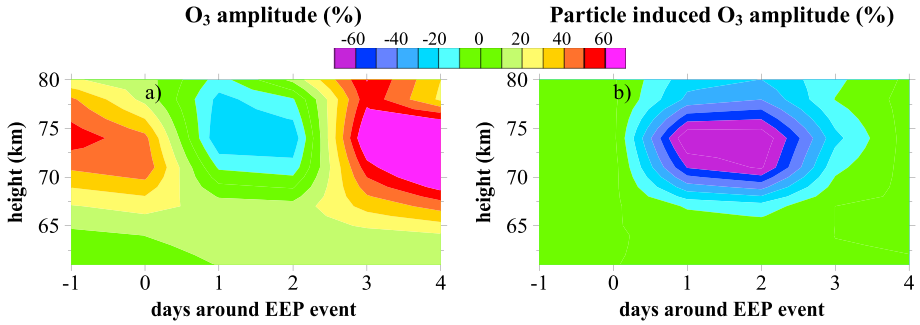

Figure 12. Amplitudes of O_3 with respect to a 7 day mean prior to the start of the EEP event (day 0) on 14 April 2006 between 55° and 75°S geomagnetic latitudes based on the (a) 3dCTM PP + F run and (b) its difference to the Base + F run.

occurrence time of the amplitudes. But the entire measured O_3 structure is shifted by a few kilometers to higher altitudes with respect to the 3dCTM results. Removing the background variability (Figure 12b) leads to intensified O_3 loss, reaching values of more than −80% and remaining for 3 days after the start of the EEP event. It is also visible that the O_3 enhancements are solely caused by dynamical variations of the background atmosphere and are not related to particle precipitation. Thus, the EEP impact on O_3 is qualitatively captured by the 3dCTM, while a substantial dynamical induced O_3 enhancement also becomes apparent.

However, no agreement was found between the O_3 amplitudes of 3dCTM PP + F run and the observations after the EEP events starting on 14 March 2003 in the SH. In this case, the particle-induced O_3 depletion is only weakly seen in the difference between PP + F run and Base + F run but completely superposed by dynamical background variations in the PP + F run. It should be pointed out that the qualitatively reproduced O_3 depletion in April 2006 is not in conflict with the strong disagreement in March 2003 in the SH. The reason is that the SH mean circulation reverses in March at these altitudes, which is usually less captured by models compared to the regular SHW conditions in April.

4. Conclusions

Simulations of the 3dCTM from January 2002 to May 2010 in the MLT region (60–133 km) were used to investigate short-term variations in atmospheric species (NO, OH, and O_3) related to geomagnetic activity (*Ap*). Geomagnetic activity was used here as a proxy for electron precipitation from the aurora and the radiation belts. Nighttime and daytime mean zonal means (55° to 75° geomagnetic latitude) of the calculated trace gas amplitudes represent the variation with respect to the corresponding background (27 day running mean). A superposed epoch analysis was applied on these trace gas amplitudes and separately carried out in the NH and SH as well as for nighttime winter and daytime summer conditions.

We found that the 27 day signal in AIMOS ionization rates is consistent with the corresponding response in *Ap*, ensuring that the general particle precipitation patterns are captured on an average. In the 3dCTM a 27 day solar rotational signal associated with precipitating particles is clearly visible in NO but only indicated in OH and O_3. However, the response in all species strongly resembles the shape and the phase of the signature in *Ap* and the AIMOS ionization rates. The patterns in the trace gases are not affected by photoionization and only weakly influenced by the 11 year solar cycle, which is caused by solar induced variations of the trace gas background.

Comparisons with published observations show that the 3dCTM does not reproduce particle related trace gas variations at altitudes <70 km due to missing electrons with energy levels >300 keV in AIMOS. Therefore, these electrons should be included in future studies. The NO patterns are reproduced with respect to the phase and shape of the measured 27 day signal. The amplitudes appear to be too strong, but this is consistent with *Ap*. The maximum response associated with the 27 day signature is more pronounced in summer (~50%) compared to winter (~30%) due to the lower NO summer background.

The response of OH and O_3 is similar in each hemisphere-season interval but strongest during SHW, agreeing with *Ap* and AIMOS ionization rate patterns in combination with a weak solar UV impact. The particle-induced enhancement of OH overlaps with O_3 depletion. Comparisons with published observations show that their

amplitudes to the magnitude of the particle events are qualitatively captured in SHW. Since even the particle impact on O_3 of a single event was reproduced, we conclude that the implemented OH-O_3 chemistry in the 3dCTM works reasonably well. In this context, we also found further support of the existence of a threshold of the magnitude of the geomagnetic event that must be exceeded before particle precipitation causes larger OH formation.

However, analyses of absolute OH variations due to particles show that OH production is overestimated by a factor of 5 in both winter hemispheres. This indicates a systematic offset, which might be caused by an unknown overestimation of AIMOS ionization rates, an overestimation of H_2O abundance during polar winter, incorrect chemical reaction rates, and the less captured dynamics in polar winter by the LIMA model. A combination of more than one of these reasons is also possible. In contrast to OH, the particle impact on O_3 is underestimated by a factor of 2 due to the lower O_3 model background, limiting O_3 loss.

We also found that O_3 amplitudes are strongly affected by dynamical induced variations of the atmospheric background in SHW. This can cause amplification or damping by more than a factor of 2 of the particle induced O_3 response. However, the former one is indicated to be the more general case when more than 100 individual events are superposed. It is probably also possible that the particle precipitation impact on O_3 after single events is completely masked by dynamics, even if it did not occur in our examples presented here. In comparison to O_3, NO, and OH amplitudes are less sensitive to dynamical related variations, probably due to their shorter chemical lifetime.

Acknowledgments

T. Fytterer, S. Bender, and M. Sinnhuber gratefully acknowledge funding by the Helmholtz Association of German Research Centers (HGF), grant VH-NG-624. H. Nieder acknowledges funding by the German Ministry for Research BMBF (grant 01LG1219C). The presented 3dCTM simulations and ENVISAT/SCIAMACHY data are not open for public so far, but access can be obtained by contacting H. Nieder (holger.nieder@kit.edu) or M. Sinnhuber (miriam.sinnhuber@kit.edu) for 3dCTM results and M. Sinnhuber or Stefan Bender (stefan.bender@kit.edu) for SCIAMACHY data. The other data used in this study are freely accessible for public and were obtained from http://www.ngdc.noaa.gov/geomag/data/poles/NP.xy (Earth's geomagnetic North Pole coordinates), http://umbra.nascom.nasa.gov/SEP/ (date and threshold of solar proton events), ftp://ftp.ngdc.noaa.gov/STP/GEOMAGNETIC_DATA/INDICES/KP_AP/ (3-hourly *ap* index values), and zonal mean wind (http://www.cpc.ncep.noaa.gov/products/stratosphere/strat-trop/).

References

Andersson, M. E., P. T. Verronen, C. J. Rodgers, M. A. Cliverd, and A. Seppälä (2014), Missing driver in the Sun-Earth connection from energetic electron precipitation impacts mesospheric ozone, *Nat. Commun.*, *5*, 5197, doi:10.1038/ncomms6197.

Andrews, D. G., J. R. Holton, and C. B. Leovy (1987), Introduction, in *Middle Atmospheric Dynamics*, *Int. Geophys. Ser.*, vol. 40, edited by R. Dmowska and J. R. Holton, pp. 1–20, Academic, Orlando, Fla.

Berger, U. (2008), Modeling of middle atmosphere dynamics with LIMA, *J. Atmos. Sol. Terr. Phys.*, *70*, 1170–1200, doi:10.1016/j.jastp.2008.02.004.

Brasseur, G. P., and S. Solomon (2005), *Aeronomy of Middle Atmosphere*, 3rd ed., Springer, Dordrecht, Netherlands.

Daae, M., P. Espy, H. Nesse Tyssøy, D. Newnham, J. Stadsnes, and F. Søraas (2012), The effect of energetic electron precipitation on middle mesospheric night-time ozone during and after a moderate geomagnetic storm, *Geophys. Res. Lett.*, *39*, L21811, doi:10.1029/2012GL053787.

Damiani, A., M. Storini, M. Laurenza, C. Rafanelli, E. Piervitali, and E. G. Cordaro (2006), Southern ozone variations induced by solar particle events during 15 January–5 February 2005, *J. Atmos. Sol. Terr. Phys.*, *68*, 2042–2052, doi:10.1016/j.jastp.2006.03.010.

Damiani, A., M. Storini, M. Laurenza, and C. Rafanelli (2008), Solar particle effects on minor components of the Polar atmosphere, *Ann. Geophys.*, *26*, 361–370, doi:10.5194/angeo-26-361-2008.

Friederich, F., M. Sinnhuber, B. Funke, T. von Clarmann, and J. Orphal (2014), Local impact of solar variation on NO_2 in the lower mesosphere and upper stratosphere from 2007 to 2012, *Atmos. Chem. Phys.*, *14*, 4055–4064, doi:10.5194/acp-14-4055-2014.

Fytterer, T., M. L. Santee, M. Sinnhuber, and S. Wang (2015), The 27 day solar rotational effect on mesospheric nighttime OH and O_3 observations induced by geomagnetic activity, *J. Geophys. Res. Space Physics*, *120*, 7926–7936, doi:10.1002/2015JA021183.

Hendrickx, K., L. Megner, J. Gumbel, D. E. Siskind, Y. J. Orsolini, H. Nesse Tyssøy, and M. Hervig (2015), Observation of the 27 day solar cycles in the production and mesospheric descent of EEP-produced NO, *J. Geophys. Res. Space Physics*, *120*, 8978–8988, doi:10.1002/2015JA021441.

Jackman, C. H., C. E. Randall, V. L. Harvey, S. Wang, E. L. Fleming, M. López-Puertas, B. Funke, and P. F. Bernath (2014), Middle atmospheric changes caused by the January and March 2012 solar proton events, *Atmos. Chem. Phys.*, *14*, 1025–1038, doi:10.5194/acp-14-1025-2014.

Laken, B. A., and J. Calogovic (2013), Composite analysis with Monte Carlo methods: An example with cosmic rays and clouds, *J. Space Weather Space Clim.*, *3*, A29, doi:10.1051/swsc/2013051.

Lean, J., G. Rottman, J. Harder, and G. Kopp (2005), Sorce contributions to new understanding of global change and solar variability, *Sol. Phys.*, *230*, 27–53, doi:10.1007/0-387-37625-9_3.

Lübken, F.-J., U. Berger, and G. Baumgarten (2013), Temperature trends in the midlatitude summer mesosphere, *J. Geophys. Res. Atmos.*, *118*, 13,347–13,360, doi:10.1002/2013JD020576.

Manney, G. L., M. J. Schwartz, K. Krüger, M. L. Santee, S. Pawson, J. N. Lee, W. H. Daffer, R. A. Fuller, and N. J. Livesey (2009), Aura Microwave Limb Sounder observations of dynamics and transport during the record-breaking 2009 Arctic stratospheric major warming, *Geophys. Res. Lett.*, *36*, L12815, doi:10.1029/2009GL038586.

Maus, S., et al. (2005), The 10th generation international geomagnetic reference field, *Phys. Earth Planet. Inter.*, *151*, 320–322, doi:10.1016/j.pepi.2005.03.006.

Nicolet, M. (1965), Ionospheric processes and nitric oxide, *J. Geophys. Res.*, *70*, 691–701, doi:10.1029/JZ070i003p00691.

Nieder, H., H. Winkler, D. R. Marsh, and M. Sinnhuber (2014), NO_x production due to energetic particle precipitation in the MLT region: Results from ion chemistry model studies, *J. Geophys. Res. Space Physics*, *119*, 2137–2148, doi:10.1002/2013JA019044.

Porter, H. S., C. H. Jackman, and A. E. S. Green (1976), Efficiencies for production of atomic nitrogen and oxygen by relativistic proton impact in air, *J. Chem. Phys.*, *65*, 154–167, doi:10.1063/1.432812.

Prather, M. J. (1986), Numerical advection by conservation of second-order moments, *J. Geophys. Res.*, *91*, 6671–6681, doi:10.1029/JD091iD06p06671.

Richardson, I. G., E. W. Cliver, and H. V. Cane (2000), Sources of geomagnetic activity over the solar cycle: Relative importance of coronal mass ejections, high-speed streams, and slow solar wind, *J. Geophys. Res.*, *105*, 18,203–18,213, doi:10.1029/1999JA000400.

Ruzmaikin, A., M. L. Santee, M. J. Schwartz, L. Froidevaux, and H. M. Pickett (2007), The 27-day variations in stratospheric ozone and temperature: New MLS data, *Geophys. Res. Lett.*, *34*, L02819, doi:10.1029/2006GL028419.

Shapiro, A. V., E. Rozanov, A. I. Shapiro, S. Wang, T. Egorova, W. Schmutz, and T. Peter (2012), Signature of the 27-day solar rotation cycle in mesospheric OH and H2O observed by Aura Microwave Limb Sounder, *Atmos. Chem. Phys.*, *12*, 3181–3188, doi:10.5194/acp-12-3181-2012.

Sinnhuber, M., J. P. Burrows, M. P. Chipperfield, C. H. Jackman, M.-B. Kallenrode, K. F. Künzi, and M. Quack (2003), A model study of the impact of magnetic field structure on atmospheric composition during solar proton events, *Geophys. Res. Lett.*, *30*(15), 1818, doi:10.1029/2003GL017265.

Sinnhuber, M., H. Nieder, and N. Wieters (2012), Energetic particle precipitation and the chemistry of the mesosphere/lower thermosphere, *Surv. Geophys.*, *33*, 1281–1334, doi:10.1007/s10712-012-9201-3.

Sinnhuber, M., S. Bender, J. P. Burrows, and F. Friederich (2016), The response of mesospheric NO to geomagnetic forcing in 2002–2012 as seen by SCIAMACHY, *J. Geophys. Res. Space Physics*, *121*, 3603–3620, doi:10.1002/2015JA022284.

Smith, A. K., et al. (2013), Satellite observations of ozone in the upper mesosphere, *J. Geophys. Res. Atmos.*, *118*, 5803–5821, doi:10.1002/jgrd.50445.

Solomon, S., D. W. Rusch, J.-C. Gérard, G. C. Reid, and P. J. Crutzen (1981), The effect of particle precipitation events on the neutral and ion chemistry of the middle atmosphere: II. Odd hydrogen, *Planet. Space Sci.*, *29*, 885–892, doi:10.1016/0032-0633(81)90078-7.

Solomon, S. C., and L. Qian (2005), Solar extreme-ultraviolet irradiance for general circulation models, *J. Geophys. Res.*, *110*, A10306, doi:10.1029/2005JA011160.

Wissing, J. M., and M.-B. Kallenrode (2009), Atmospheric Ionization Module Osnabrück (AIMOS): A 3-D model to determine atmospheric ionization by energetic charged particles from different populations, *J. Geophys. Res.*, *114*, A06104, doi:10.1029/2008JA013884.

Wissing, J. M., M.-B. Kallenrode, N. Wieters, H. Winkler, and M. Sinnhuber (2010), Atmospheric Ionization Module Osnabrück (AIMOS): 2. Total particle inventory in the October–November 2003 event and ozone, *J. Geophys. Res.*, *115*, A02308, doi:10.1029/2009JA014419.

Wissing, J. M., M.-B. Kallenrode, J. Kieser, H. Schmidt, M. T. Rietveld, A. Strømme, and P. J. Erickson (2011), Atmospheric Ionization Module Osnabrück (AIMOS): 3. Comparison of electron density simulations by AIMOS-HAMMONIA and incoherent scatter radar measurements, *J. Geophys. Res.*, *116*, A08305, doi:10.1029/2010JA016300.